Microscopic magnetic modeling for the $S = \frac{1}{2}$ alternating-chain compounds $Na_3Cu_2SbO_6$ and $Na_2Cu_2TeO_6$

M. Schmitt,[1,2] O. Janson,[1,3] S. Golbs,[1] M. Schmidt,[1] W. Schnelle,[1] J. Richter,[4] and H. Rosner[1,*]

[1]*Max-Planck-Institut für Chemische Physik fester Stoffe, Nöthnitzer Strasse 40, 01187 Dresden, Germany*

[2]*Fachbereich Physik, Technische Universität Kaiserslautern, 67663 Kaiserslautern, Germany*

[3]*National Institute of Chemical Physics and Biophysics, 12618 Tallinn, Estonia*

[4]*Institut für Theoretische Physik, Universität Magdeburg, 39016 Magdeburg, Germany*

(Received 5 February 2014; revised manuscript received 14 April 2014; published 2 May 2014)

The spin-1/2 alternating Heisenberg chain system $Na_3Cu_2SbO_6$ features two relevant exchange couplings: J_{1a} within the structural Cu_2O_6 dimers and J_{1b} between the dimers. Motivated by the controversially discussed nature of J_{1a}, we perform extensive density-functional-theory (DFT) calculations, including DFT + U and hybrid functionals. Fits to the experimental magnetic susceptibility using high-temperature series expansions and quantum Monte Carlo simulations yield the optimal parameters $J_{1a} = -217$ K and $J_{1b} = 174$ K with the alternation ratio $\alpha = J_{1a}/J_{1b} \simeq -1.25$. For the closely related system $Na_2Cu_2TeO_6$, DFT yields substantially enhanced J_{1b}, but weaker J_{1a}. The comparative analysis renders the buckling of the chains as the key parameter altering the magnetic coupling regime. Numerical simulation of the dispersion relations of the alternating-chain model clarify why both antiferromagnetic and ferromagnetic J_{1a} can reproduce the experimental magnetic susceptibility data.

DOI: 10.1103/PhysRevB.89.174403 PACS number(s): 75.50.Ee, 71.70.Gm, 71.15.Mb, 75.10.Jm

I. INTRODUCTION

The vibrant research on magnetic insulators keeps on delivering new examples of exotic magnetic behaviors and unusual magnetic ground states (GSs) [1,2]. Two prominent examples are the spin-liquid system herbertsmithite $Cu_3Zn(OH)_6Cl_2$, featuring a kagome lattice of $S = 1/2$ spins [3], or the recently discovered $Ba_3CuSb_2O_9$, where the magnetism is likely entangled with the dynamical Jahn-Teller distortion [4].

Cuprates are a particularly promising playground to study low-dimensional magnetism, since they often combine the quantum spin $S = 1/2$ ensured by the Cu $3d^9$ electron configuration and the low dimensionality of the underlying magnetic model. The latter is ensued by the unique variety of lattice topologies realized in cuprates, which includes geometrically frustrated lattices, where quantum fluctuations are additionally enhanced by the competing magnetic interactions.

The simplest example of a quantum GS that lacks a classical analog is the quantum-mechanical singlet. Such a GS is found experimentally, e.g., in CsV_2O_5 (Ref. [5]), $CuTe_2O_5$ (Ref. [6]), $CaCuGe_2O_6$ (Ref. [7]), and $Cu_2(PO_3)_2CH_2$ (Ref. [8]). All these compounds feature pairs of strongly coupled spins (magnetic dimers). An isolated dimer is an archetypical two-level quantum system, which can be solved analytically.

Compounds with sizable couplings between the dimers can exhibit diverse behaviors. For instance, the nonfrustrated [9] spin lattice of the Han purple $BaCuSi_2O_6$ is favorable for propagation of triplet excitations, promoting a Bose-Einstein condensation of magnons, experimentally observed in the magnetic field range between 23.5 and 49 T [10]. In contrast, $SrCu_2(BO_3)_2$ features strongly frustrated interdimer couplings that give rise to a fascinating variety of magnetization plateaus [11]. The remarkable difference between the behavior of $BaCuSi_2O_6$ and $SrCu_2(BO_3)_2$ is governed by the difference in the magnetic couplings that constitute the respective spin model. Thus, the precise information on the underlying spin model is crucial for understanding the magnetic properties.

An evaluation of the microscopic magnetic model can be performed in different ways. The basic features of the spin lattice can be often conceived by applying empirical rules, such as the Goodenough-Kanamori rules [12]. Then, the resulting qualitative model is parametrized by fitting its respective free parameters to the experiment. The main challenge is the limited amount of the available experimental data that may not suffice for a unique and justified fitting of the model-specific free parameters. Thus, such a phenomenological approach is generally insecure against ambiguous solutions.

Microscopic modeling based on density-functional theory (DFT) calculations is an alternative solution. Such calculations require no experimental information beyond the crystal structure, and in contrast to the phenomenological method, provide a microscopic insight. A straightforward application of the DFT is impeded by the fact that cuprates are strongly correlated materials. Hence the effective one-electron approach of DFT generally fails to reproduce their insulating electronic GS [13]. This shortcoming can be mended in alternative calculational schemes, such as DFT + U or hybrid functionals, yet these methods are not parameter free. Often, these parameters sensitively depend on the fine structural details of the system under investigation.

The low-dimensional $S = 1/2$ Heisenberg compound $Na_3Cu_2SbO_6$ is an instructive example that demonstrates the performance and the limitations of the phenomenological as well as the microscopic approach. This compound was initially described as a distorted honeycomb lattice, owing to the hexagonal arrangement of the Cu atoms in the crystal structure [14]. However, this purely geometrical analysis neglects the key ingredients of the magnetic superexchange, such as the orientation and the spatial extent of the magnetically active orbitals. Indeed, as pointed out by the authors of Ref. [14], the orientation of the Cu $3d_{x^2-y^2}$ orbitals readily

*rosner@cpfs.mpg.de

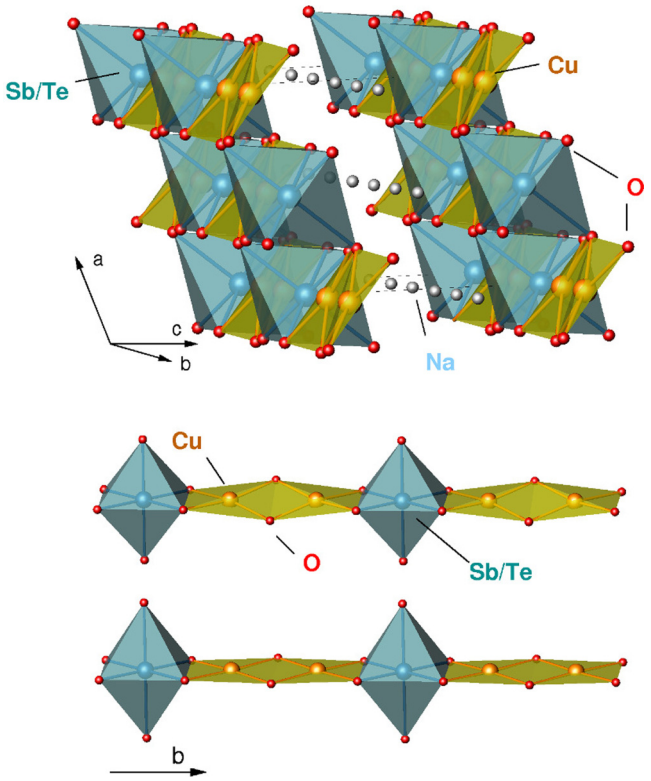

FIG. 1. (Color online) Top: crystal structure of $Na_3Cu_2SbO_6$. The basic elements are CuO_4 plaquettes and SbO_6 octahedra. Bottom: segments of the structural chains of Cu_2O_6 dimers for the experimental distorted plaquette geometry (upper panel) and an ideal planar arrangement of the Cu_2O_6 units in the fictitious structures (lower panel).

accentuates the chains formed by structural dimers and hints at two relevant magnetic couplings: J_{1a} within the structural dimers and J_{1b} between the dimers (Fig. 1), leading to the quasi-1D Heisenberg chain model with alternating nearest-neighbor couplings.

Thermodynamical measurements confirmed the quasi-1D character of the spin model [14,15], yet no agreement was found for the sign of the intradimer coupling J_{1a}: Refs. [14] and [15] vouch for a ferromagnetic (FM) and antiferromagnetic (AFM) exchange, respectively. The sign of J_{1a} basically governs the magnetic GS: the AFM-AFM solution is a disordered dimer state, while the GS of an FM-AFM chain is adiabatically connected to the Haldane phase with nontrivial topology and sizable string order parameter [16]. Therefore, for the magnetic GS, the sign of J_{1a} is of crucial importance.

Notably, even DFT studies do not concur with each other: Ref. [15] reports AFM J_{1a}, while an alternative DFT-based method in Ref. [17] yields FM coupling. To resolve the controversy on the sign of J_{1a}, the authors of Ref. [18] performed inelastic neutron scattering (INS) experiments on single crystals of $Na_3Cu_2SbO_6$. The resulting values for the exchange couplings ($J_{1a} = -145$ K and $J_{1b} = 161$ K) clearly indicate the FM-AFM chain scenario. Still, the origin of ambiguous solutions in earlier experimental as well as in DFT studies has not been sufficiently clarified.

In our combined experimental and theoretical study, we evaluate the magnetic model for $Na_3Cu_2SbO_6$ and its Te sibling $Na_2Cu_2TeO_6$ (Ref. [19]) using extensive DFT calculations and investigate how the magnetic GS is affected by the structural distortion within the chains. By comparing our DFT results to the earlier studies, we explain the origin of ambiguous parametrizations of DFT-based spin models in both compounds. Simulations of the momentum-resolved spectrum for our microscopic model reveal excellent agreement with the INS experiments (Ref. [18]) and enlighten the ambiguity of AFM-AFM and FM-AFM solutions inferred from the thermodynamical measurements.

This paper is organized as follows. The used experimental as well as computational methods are described in Sec. II. The details of the crystal structures of $Na_3Cu_2SbO_6$ and $Na_2Cu_2TeO_6$ are discussed in Sec. III. In Sec. IV, we present our magnetic susceptibility measurements and extensive DFT calculations. Peculiarities of the excitation spectrum of the Heisenberg chain model are discussed Sec. V. Finally, a summary and a short outlook are given in Sec. VI.

II. METHODS

Synthesis and sample characterization. Polycrystalline samples of $Na_3Cu_2SbO_6$ were prepared by solid-state reaction. A stoichiometric amount of Na_2CO_3 (Chempur, 99.9 + %), Sb_2O_5 (99.999%, Alfa Aesar), and $CuCO_3{\cdot}Cu(OH)_2$ (Chempur) was thoroughly mixed. The homogeneous powder was pressed into a platinum crucible and annealed at 1273 K for two weeks in air. Finally the crucible was taken out of the furnace at 1273 K and cooled down to room temperature in air.

For magnetic measurements, the powder sample was pressed into a pellet and heated again at 973 K in a platinum boat for several days. The green powder was identified and characterized by powder x-ray diffraction using a high-resolution Guinier camera with Cu K_α radiation. The determined lattice parameters $a = 5.676$ Å, $b = 8.860$ Å, $c = 5.833$ Å, and $\beta = 113.33^\circ$ are in good agreement with Ref. [20].

To control the oxygen content in the sample at different stages of the thermal treatment, we performed coulometric titration of the samples using a commercial OXYLYT device. We found that the maximal oxygen content (close to the stoichiometric $Na_3Cu_2SbO_6$) is attained right after the thermal treatment at 973 K (Fig. S3 in Ref. [21]). However, a subsequent storage at room temperature and in air leads to a reduction of the oxygen content. This effect can be seen in the magnetic susceptibility by the increased amount of Curie impurity (Fig. S4 in Ref. [21]). Therefore, for thermodynamic measurements, we use "fresh" samples (i.e., we performed measurement right after the thermal treatment) that feature smallest impurity contribution. Magnetic susceptibility $\chi(T)$ of $Na_3Cu_2SbO_6$ was measured using a superconducting quantum interference device (SQUID) magnetometer (MPMS, Quantum Design) in a magnetic field of 0.04 T.

DFT calculations. For the electronic structure calculations, the full-potential local-orbital code FPLO (version FPLO8.50-32) within the local (spin) density approximation [L(S)DA] was

used [22]. In the scalar relativistic calculations the exchange and correlation potential of Perdew and Wang has been applied [23]. The accuracy with respect to the k-mesh has been carefully checked.

The LDA band structure has been mapped onto an effective one-orbital tight-binding (TB) model based on Cu-site centered Wannier functions (WFs). The strong Coulomb repulsion of the Cu $3d$ orbitals was considered by mapping the TB model onto a Hubbard model. In the strongly correlated limit and at half filling, the lowest-lying (magnetic) excitations can be described by a Heisenberg model with $J_{ij}^{\mathrm{AFM}} = 4t_{ij}^2/U_{\mathrm{eff}}$ for the antiferromagnetic part of the exchange. Spin-polarized LSDA + U supercell calculations were performed using two limiting cases for the double counting correction (DCC): the around-mean-field (AMF) and the atomic limit (AL, also called the fully localized limit). We varied the on-site Coulomb repulsion U_{3d} in the physically relevant range (4–8 eV in AMF and 5–9 eV in AL), keeping the on-site exchange $J_{3d} = 1$ eV. The partial Na_{3-x} occupancy and the Sb_x/Te_{1-x} substitution were modeled using the virtual crystal approximation (VCA) [24].

HSE06 (Ref. [25]) hybrid functional calculations were performed using the pseudopotential code VASP-5.2 [26], employing the basis set of projector-augmented waves. The default admixture of the Fock exchange (25%) was adopted. We used the primitive unit cell with two Cu atoms and a $6\times6\times6$ k-mesh with the NKRED = 3 flag.

Simulations and fits to the experiment. We used the high-temperature series expansion (HTSE) to a Heisenberg chain with alternating nearest-neighbor couplings J_{1a} and J_{1b}. For the case of AFM couplings, the parametrization is given in $\alpha \equiv |J_{1a}|/J_{1b}$ in Table II of Ref. [27]; the parameters for the case of FM J_{1a} are provided in Ref. [28]. Quantum Monte Carlo simulations were performed using the LOOP algorithm [29] from the ALPS package [30]. To evaluate the reduced magnetic susceptibility, we used 50 000 loops for thermalization and 500 000 loops after thermalization for chains of $N = 120$ spins $S = 1/2$ using periodic boundary conditions. Exact (Lanczos) diagonalization of the Heisenberg Hamiltonians was performed using SPINPACK [31]. The lowest-lying $S^z = 0$, $S^z = 1$, and $S^z = 2$ excitations were computed for $N = 32$ sites chains of $S = 1/2$ using periodic boundary conditions.

III. CRYSTAL STRUCTURE

The monoclinic (space group $C2/c$) crystal structure of $Na_3Cu_2SbO_6$ (Ref. [20]) features pairs of slightly distorted, edge-shared CuO_4 plaquettes forming structural dimers with the Cu-O-Cu bonding angle of 95°. The dimers are connected by the equatorial plane of SbO_6 octahedra and form chains running along the b axis (Fig. 1, bottom). The apical O atoms of the SbO_6 octahedra mediate connections to the next Cu_2O_6 dimer chain. In this way, the magnetic layers, separated by Na atoms, are formed (Fig. 1, top).

The crystal structure of $Na_2Cu_2TeO_6$ (Ref. [19]) features a similar motif, with the reduced number of Na atoms between the layers, to keep the charge balance. In addition, the smaller size of Te^{6+} compared to Sb^{5+} gives rise to a stronger distortion of the Cu_2O_6 dimer chains in $Na_2Cu_2TeO_6$. To investigate the influence of this distortion, we also computed fictitious structures with idealized planar arrangements of the Cu_2O_6 units (Fig. 1 bottom, lower panel).

IV. RESULTS

A. Magnetic susceptibility

Above 200 K, the magnetic susceptibility of $Na_3Cu_2SbO_6$ fits reasonably to the Curie-Weiss law with $C = 0.442$ emu K(mol Cu)$^{-1}$ and the antiferromagnetic Weiss temperature $\theta_{\mathrm{CW}} = 60 \pm 10$ K. The effective magnetic moment amounts to $\mu_{\mathrm{eff}} \simeq 1.88\mu_{\mathrm{B}}$, slightly exceeding the spin-only value for $S = 1/2$ ($1.73\mu_{\mathrm{B}}$). The resulting value of the Lande factor $g = 2.17$ is typical for Cu^{2+} compounds. At lower temperatures, antiferromagnetic correlations give rise to a broad maximum in the magnetic susceptibility around $T_{\mathrm{max}} = 96$ K. The low-temperature upturn below 17 K is likely caused by defects, typical for powder samples of quasi-one-dimensional magnets [e.g., $Sr_2Cu(PO_4)_2$ from Ref. [32] or $(NO)Cu(NO_3)_3$ from Ref. [33]], since already a single defect terminates the spin chain.

We briefly compare our susceptibility measurements with the published data. The Curie-Weiss fit from Ref. [15] yields a similar $\theta_{\mathrm{CW}} = 55$ K, but their $g = 2.33$ exceeds our estimate. This discrepancy likely originates from the difference in the magnetic field (0.1 T vs 0.04 T in our work) as well as different temperature ranges used for the fitting. Unfortunately, the authors of Ref. [14] do not provide the values of θ_{CW} and g, but a Curie-Weiss fit to their data yields $\theta_{\mathrm{CW}} \simeq 49$ K and $g \simeq 2.10$, in good agreement with our findings. A bare comparison of the absolute values of $\chi(T_{\mathrm{max}})$ (Table I) reveals sizable deviations of the $\chi(T)$ data from Ref. [15] compared to the other two data sets.

For a more elaborate analysis, we adopt the AHC model and search for solutions that agree with the experimental $\chi(T)$ curve. To this end, we perform HTSE considering the physically different scenarios: both J_{1a} and J_{1b} couplings are AFM ("AFM-AFM") and J_{1a} is FM ("FM-AFM"). The corresponding HTSE coefficients for the two cases can be found in Refs. [27] and [28], respectively. In both cases, we obtain a solution (first row of Table II) which conforms to the experimental data.

Our solution for the FM-AFM case (Table II, first row) nearly coincides with the corresponding solution from Ref. [14] (Table II, second row), yielding $\alpha \equiv J_{1a}/J_{1b} \simeq -1.25$ and a considerably smaller g factor of about 2 compared to the value from the Curie-Weiss fits (2.17). For the AFM-AFM case, we obtain $\alpha \simeq 0.4$ which deviates from the result of Ref. [14], but closely resembles the solution from

TABLE I. $Na_3Cu_2SbO_6$: the Curie-Weiss temperature θ_{CW} (in K) and the g factor evaluated using the Curie-Weiss fit for $T \geqslant 200$ K, as well as the experimental position T_{max} (in K) of the susceptibility maximum and its absolute value $\chi(T_{\mathrm{max}})$ [in emu (mol Cu)$^{-1}$].

Data source	θ_{CW}	g	T_{max}	$\chi(T_{\mathrm{max}})$
This study	60	2.17	96	2.2×10^{-3}
Data from Ref. [14]	49	2.10	95	2.3×10^{-3}
Ref. [15]	55	2.33	90	1.7×10^{-3}

TABLE II. High-temperature series expansion (HTSE) and quantum Monte Carlo (QMC) fits to the experimental $\chi(T)$ data for $Na_3Cu_2SbO_6$. Results of different studies implying a ferromagnetic and an antiferromagnetic coupling (FM-AFM, upper lines) or two inequivalent antiferromagnetic couplings (AFM-AFM, lower lines) are shown: exchange couplings J_{1a} and J_{1b} (in K), g factors, temperature-independent terms χ_0[in emu/(mol Cu)$^{-1}$], and Curie-Weiss impurity contributions $C^{\rm imp}$ [in K emu (mol Cu)$^{-1}$] and $\theta_{\rm CW}^{\rm imp}$ (in K). "–" stands for a fitted quantity, which numerical value is not provided in the respective reference.

	J_{1a}	J_{1b}	g	χ_0	$C^{\rm imp}$	$\theta_{\rm CW}^{\rm imp}$
			HTSE			
This study	−207	171	2.01	3×10^{-5}	4.7×10^{-3}	
	155	66	2.20	3×10^{-6}	6.1×10^{-3}	1.1
Ref. [14]	−209	165	2.01	–	–	–
	143	39	2.13	–	–	–
Ref. [15]	160	62	1.97	2.2×10^{-4}		2.3
			QMC			
This study	−217	174	2.02	9×10^{-6}	6×10^{-3}	1
	153	61	2.19	3×10^{-6}	6×10^{-3}	1.2

Ref. [15] (Table II, third row). The discrepancy can originate from different parametrizations used for the HTSE fitting. In particular, the AFM-AFM solutions in Refs. [14] and [15] are obtained using the parametrization from Ref. [34]. In contrast, we adopt the coefficients from a more recent and extensive study [27], valid in the whole temperature range measured.

To account for the full temperature range measured, we turn to QMC simulations. Thus, we adopt the ratios $\alpha = -1.25$ and $\alpha = 0.40$ from our HTSE fitting, and calculate the reduced magnetic susceptibility $\chi^*(T/k_BJ)$, which can be fitted to the experimental curve using the expression

$$\chi(T) = \frac{N_A g^2 \mu_B^2}{k_B J}\chi^*\left(\frac{T}{k_B J}\right) + \frac{C^{\rm imp}}{T+\theta_{\rm CW}^{\rm imp}} + \chi_0, \qquad (1)$$

where N_A and k_B are the Avogadro and Boltzmann constants, respectively, μ_B is the Bohr magneton, $C^{\rm imp}$ and $\theta_{\rm CW}^{\rm imp}$ account for impurity/defect contributions, χ_0 is a temperature-independent term, and $J = \max\{|J_{1a}|, J_{1b}\}$. Using a least-squares fitting, we obtain the solutions listed in Table II (last row) and shown in Fig. 2.

The AFM-AFM solution shows sizable deviations at high temperatures and in the vicinity of the low-temperature upturn (Fig. 2, inset), while the FM-AFM solution yields an excellent fit to the experimental $\chi(T)$ in the whole temperature range, making the latter solution more favorable. Still, the choice is impeded by the following issues. First, the AHC model is a minimal model for $Na_3Cu_2SbO_6$, which completely neglects interchain couplings and anisotropies. Second, the g factor of the FM-AFM solution deviates significantly from the estimate based on the Curie-Weiss fit, while its counterpart from the AFM-AFM solution shows a better agreement with the Curie-Weiss fit. Finally, the shape of the $\chi(T)$ curve is affected by oxygen deficiency in the sample [21], which is difficult to control during the synthesis process. Therefore, the AFM-AFM solution cannot be ruled out using the $\chi(T)$ data, only.

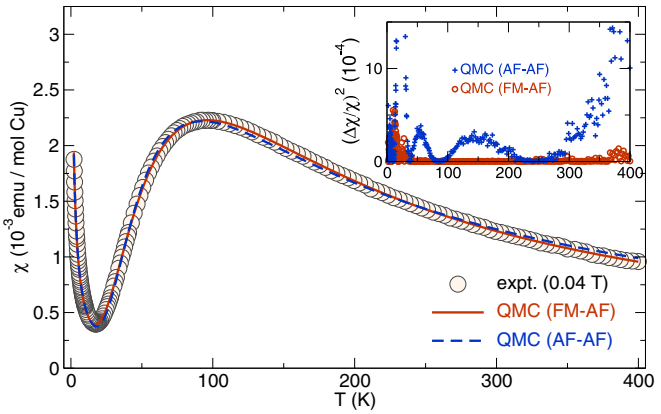

FIG. 2. (Color online) Experimental (expt.) magnetic susceptibility of $Na_3Cu_2SbO_6$ (circles) and the quantum Monte Carlo (QMC) fits for the FM-AFM and the AFM-AFM solution of the alternating Heisenberg chain (AHC) model. Inset: difference curves emphasize the excellence of the FM-AFM solution.

B. Electronic structure and magnetic model

To resolve the ambiguity between the FM-AFM and AFM-AFM solutions, we perform microscopic magnetic modeling of $Na_3Cu_2SbO_6$ and its Te sibling $Na_2Cu_2TeO_6$ using DFT calculations. The valence bands feature similar bandwidth and are similarly structured in the two compounds, as revealed by the LDA densities of states (DOS) in Fig. 3. The DOS is dominated by Cu and O states down to −5.5 and −6 eV for $Na_3Cu_2SbO_6$ and $Na_2Cu_2TeO_6$, respectively. Contributions from Na, Sb, and Te are marginal in this energy range. Only at the lower edge of the valence band do we find a sizable hybridization of Sb states for $Na_3Cu_2SbO_6$ centered around −6 eV. A similar admixture of Te states is observed for $Na_2Cu_2TeO_6$, where the additional valence electron of Te compared to Sb shifts the Cu-O-Te density down by about 1 eV.

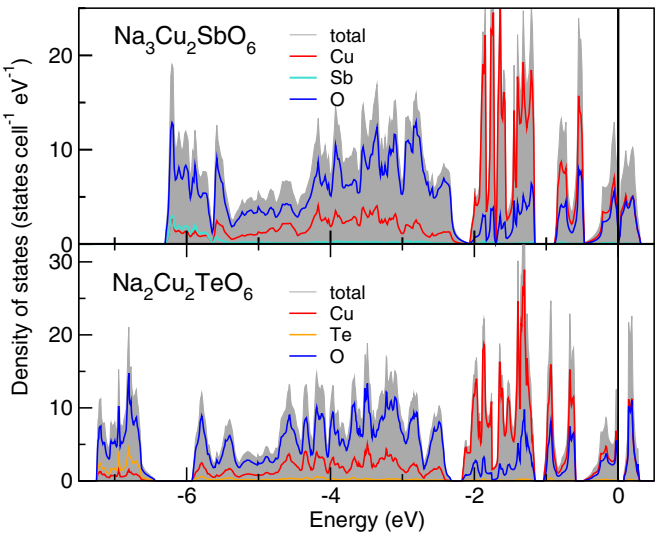

FIG. 3. (Color online) Total and atom-resolved LDA density of states for $Na_3Cu_2SbO_6$ (top) and $Na_2Cu_2TeO_6$ (bottom). The contribution of Na states is negligible on this scale (not shown).

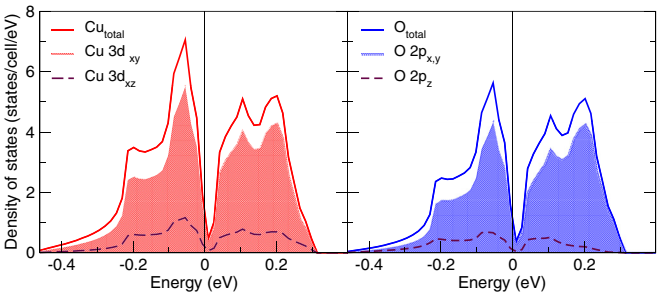

FIG. 4. (Color online) Orbital-resolved LDA density of states for $Na_3Cu_2SbO_6$. In the local coordinate system of a CuO_4 plaquette, the x axis runs along one of the Cu-O bonds, while the z axis is perpendicular to the plaquette plane (for the ideal planar coordination). The states in the vicinity of the Fermi energy are dominated by the in-plane Cu $3d$ and O $2p$ states.

The LDA band structures for both compounds feature a well-separated density of Cu and O states centered around the Fermi energy. In the local coordinate system of a CuO_4 plaquette, this density is formed by the antibonding σ combination of Cu $3d_{x^2-y^2}$ and O $2p_\sigma$ states ($dp\sigma^*$ combination). The orbital-resolved density of states for $Na_3Cu_2SbO_6$ is shown in Fig. 4. Two aspects should be pointed out. First, the metallic solution (nonzero DOS at the Fermi energy) observed in $Na_3Cu_2SbO_6$, is in contrast with the green color of the compound, indicative of the insulating behavior. Similar, the calculated LDA band gap of 0.06 eV for $Na_2Cu_2TeO_6$ (see Fig. 3) is far too small to account for the green color of the powder and originates from dimerization effects. This drastic underestimation of the band gap is a well-known shortcoming of the LDA, which does not account for the strong Coulomb repulsion in the Cu $3d$ orbitals. The missing part of correlation energy will be accounted for by resorting to a Hubbard model, as well as using DFT + U and hybrid-functional calculations. Second, the orbital resolved density of states (see Fig. 4) shows small hybridization with the out-of-plane Cu-O states due to the distortion of the dimer chains. Since these contributions are small compared to the pure antibonding $dp\sigma^*$ states, the restriction to an effective TB model is still justified.

To verify the structural input, we relaxed the crystal structures within LDA. For $Na_3Cu_2SbO_6$, the relaxation results in a rather small energy gain of 33 meV per formula unit (f.u.), and the respective changes in the crystal structure are negligible. In contrast, a relaxation of the atomic coordinates in $Na_2Cu_2TeO_6$ lowers the energy by 130 meV per f.u. and alters mainly the chain buckling. Since the relaxation of $Na_2Cu_2TeO_6$ affects the magnetically relevant $dp\sigma^*$ states, we evaluated the magnetic properties for both the experimental and the relaxed crystal structure.

The transfer integrals t_{ij} (the hopping matrix elements) are evaluated by a least-squares fit of an effective one-orbital TB model to the two LDA $dp\sigma^*$ bands. Using ten inequivalent t_{ij} terms (see the bottom panel of Fig. 5, Table III, and Ref. [21]) we obtain excellent agreement between the TB model and the LDA band structure. The respective fit for $Na_3Cu_2SbO_6$ is shown in Fig. 5 (top).

In both systems, the leading coupling is t_{1b}, which connects two neighboring structural dimers: $t_{1b} = 127$ meV for

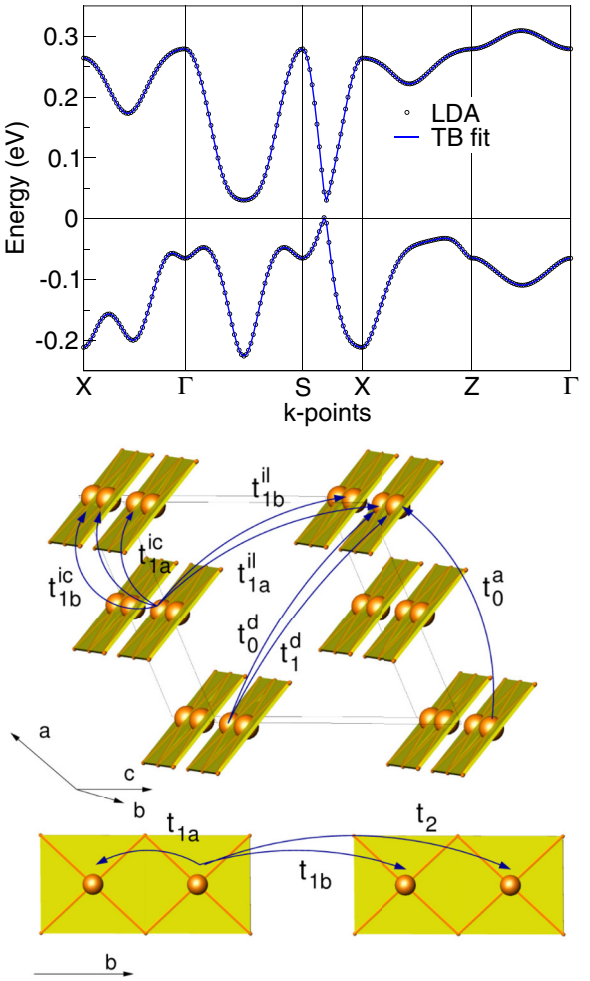

FIG. 5. (Color online) Top: LDA band structure of $Na_3Cu_2SbO_6$ and the fit using the effective one-orbital TB model with ten inequivalent transfer integrals t_{ij}. Bottom: the superexchange pathways corresponding to the relevant t_{ij} terms.

$Na_3Cu_2SbO_6$ and $t_{1b} = 162$ meV for $Na_2Cu_2TeO_6$, respectively. The coupling within the structural Cu_2O_6 dimers ($t_{1a} = 60$ meV for $Na_3Cu_2SbO_6$ and $t_{1a} = 16$ meV for $Na_2Cu_2TeO_6$)

TABLE III. Relevant (>10 meV) transfer integrals t_{ij} (in meV) evaluated by fitting the LSDA band structures for the different structural models: experimental (expt), LSDA-relaxed (relaxed) and fictitious planar (planar). For the notation of t_{ij}, see Fig. 5 (bottom).

$Na_3Cu_2SbO_6$							
t_i/meV	t_{1a}	t_{1b}	t_2	t^{ic}_{1a}	t^{ic}_{1b}	t^{d}_{0}	t^{a}_{0}
Expt.	**60.6**	**127**	18.2	−27.8	17.0	21.8	17.4
Relaxed	**68.2**	**134**	18.1	−32.3	20.6	20.9	19.2
Planar expt.	**45.3**	**119**	22.4	−7.8	9.4	30.1	–
Planar relax.	**55.6**	**125**	23.8	−9.2	10.7	29.2	–
$Na_2Cu_2TeO_6$							
t_i/meV	t_{1a}	t_{1b}	t_2	t^{ic}_{1a}	t^{ic}_{1b}	t^{d}_{0}	t^{a}_{0}
Expt.	**15.6**	**162**	16.4	−38.5	24.7	13.7	25.5
Relaxed	**42.5**	**152**	17.3	−42.4	26.3	14.5	23.1
Planar expt.	**27.3**	**152**	29.3	−12.6	12.4	25.6	1.3
Planar relax.	**45.2**	**148**	30.0	−12.8	12.7	26.0	–

are significantly smaller. Besides, several long-range couplings that connect different chains are comparable to t_{1a} (Table III and Ref. [21]). Subsequent mapping of the TB model onto a Hubbard model (adopting $U_{\rm eff} = 4$ eV) and a Heisenberg model yield the following AFM contributions: $J_{1b}^{\rm AFM} = 188$ K and $J_{1a}^{\rm AFM} = 43$ K for $Na_3Cu_2SbO_6$ and $J_{1b}^{\rm AFM} = 305$ K and $J_{1a}^{\rm AFM} = 2$ K for $Na_2Cu_2TeO_6$, respectively.

The resulting minimal model is incomplete, since it disregards the FM contribution to the exchange integrals, which are expected to be especially large for the J_{1a} coupling within the structural dimers. To estimate the total exchange integrals, comprising AFM and FM contributions, we performed LSDA + U calculations of magnetic supercells. Mapping the total energies of different collinear spin arrangements onto a classical Heisenberg model yields $J_{1a} = -135 \pm 20$ K for $Na_3Cu_2SbO_6$ and $J_{1a} = -120 \pm 20$ K for $Na_2Cu_2TeO_6$, respectively. For the exchange between the structural dimers, we find $J_{1b} = 150 \pm 50$ K for $Na_3Cu_2SbO_6$ and $J_{1b} = 232 \pm 70$ K for $Na_2Cu_2TeO_6$ ($U_{3d} = 6 \mp 1$ eV). All further exchange integrals between different chains and layers are smaller than 10 K, and thus can be neglected in the minimal model.

Unlike the related compounds featuring edge-shared chains [35,36] or Cu_2O_6 dimers [8], $Na_3Cu_2SbO_6$ and $Na_2Cu_2TeO_6$ exhibit a sizable influence of the Coulomb repulsion U_{3d} on the exchange integrals (see Fig. 6). However, the variation of U_{3d} within the physically relevant range (Sec. II) does not affect the FM nature of J_{1a}. Thus, $Na_3Cu_2SbO_6$ features

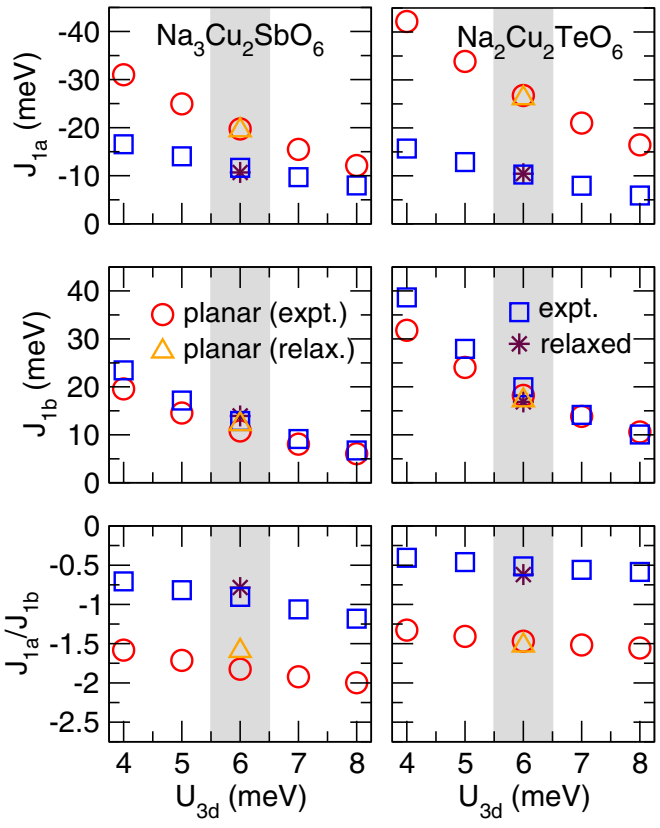

FIG. 6. (Color online) Calculated exchange integrals J_{1b} and J_{1a}, as well as frustration ratios $J_{1a}/J_{1b} = \alpha$ as a function of the Coulomb repulsion U_{3d} for different structural models of the two compounds.

TABLE IV. Leading exchange integrals J_{1a} and J_{1b} (in K) and the alternation ratio $\alpha \equiv J_{1a}/J_{1b}$ for $Na_3Cu_2SbO_6$ and $Na_2Cu_2TeO_6$, evaluated using different methods. HTSE and QMC estimates are made based on the experimental data from the respective reference (first column). Theoretical estimates, LSDA + U, HSE06, and extended Hückel tight-binding (EHTB) results are based on calculations for the experimental crystal structures.

Data source	Method	J_{1a}	J_{1b}	$\alpha = J_{1a}/J_{1b}$
		$Na_3Cu_2SbO_6$		
This study	LSDA + U	−135	150	−0.90
	HSE06	−205	163	−1.26
	HTSE	−207	171	−1.21
	QMC	−217	174	−1.25
Ref. [17]	EHTB	−165	345	−0.48
Ref. [14]	HTSE	−165	209	−0.79
Ref. [15]	HTSE	22	169	0.13
		$Na_2Cu_2TeO_6$		
This study	LSDA + U	−120	232	−0.52
	HSE06	−165	291	−0.57
Ref. [17]	EHTB	−158	516	−0.30
Ref. [14]	HTSE	−272	215	−1.27
Ref. [19]	HTSE	13	127	0.1

alternating chains with the exchange integrals of nearly the same magnitude but different sign (FM J_{1a} and AFM J_{1b}), while for $Na_2Cu_2TeO_6$, the AFM exchange between the structural dimers is dominant. The evaluated exchange integrals are listed in Table IV.

For an independent computational method, we use hybrid functional (HF) total energy calculations. The absence of the double counting problem and minimal number of free parameters makes HF calculations an appealing alternative to the DFT + U methods [37]. Here, we employ the HSE06 functional to evaluate the leading couplings J_{1a} and J_{1b} in both compounds. In accord with DFT + U, we obtain FM J_{1a} and AFM J_{1b}. For $Na_3Cu_2SbO_6$, the resulting exchange integrals are in excellent agreement with the HTSE estimates (Table IV). Similar to DFT + U, $Na_2Cu_2TeO_6$ features a weaker J_{1a} and stronger J_{1b}, thus the α value is substantially reduced.

We are now in position to compare our results with the previous DFT-based studies. Derakhshan *et al.* (Ref. [15]) evaluated the relevant transfer integrals using Nth-order muffin-tin-orbital downfolding of the LDA band structure. Although this computational method (Ref. [38]) as well as the code [39] used for the calculations differ from our approach, the difference in the resulting t_{ij} values does not exceed 25% [40]. Hence, the estimated AFM contributions to the exchanges J_{1a} and J_{1b} generally agree with our values. However, in contrast to the present study, the authors of Ref. [15] did not perform DFT + U calculations and therefore completely disregarded the FM contributions, which are especially relevant for the short-range coupling J_{1a}. Thus, their AFM-AFM solution originates from a severe incompleteness of the computational scheme and the respective mapping onto the spin Hamiltonian.

In contrast to Ref. [17], Koo and Whangbo performed DFT + U calculations using VASP, and recovered FM J_{1a} and AFM J_{1b}, in qualitative agreement with the experiment.

However, the absolute values of the leading couplings are considerably overestimated. We believe that this overestimation stems from the choice of the on-site Coulomb repulsion parameter U_d. It is well known that the parameters of the DFT + U calculations are not universal [41], in particular basis dependent, and should be carefully chosen based on the nature of the magnetic atom and the code used. The U_d range studied in Ref. [17] (4–7 eV) is too narrow, and larger U_d is likely required to reproduce the correct magnetic energy scale in $Na_3Cu_2SbO_6$ and $Na_2Cu_2TeO_6$.

C. Influence of chain geometry

Next, we study the influence of the structural parameters onto the alternation ratio $\alpha = J_{1a}/J_{1b}$ for $Na_3Cu_2SbO_6$ and $Na_2Cu_2TeO_6$. The two compounds differ not only by the nonmagnetic ions (Sb and Te) located between the structural dimers, but also by details of their chain geometry. These subtle differences can have a substantial impact on the magnetic properties. In particular, the substitution of Sb by Te and the corresponding change of the Na content modulates the crystal field. Furthermore, the substitution of Sb by Te has a sizable impact on the buckling of the dimer chains, which is determined by the deviation of O atoms from an ideal planar arrangement. Finally, the interatomic distances in the two compounds are different. To separate these effects out, we introduce fictitious compounds containing ideal planar dimer chains (see Fig. 1), evaluate their electronic structure, and compare them with real compounds.

The direct comparison of the antibonding $dp\sigma^*$ bands for the experimentally observed crystal structures of $Na_3Cu_2SbO_6$ and $Na_2Cu_2TeO_6$ (Fig. 7, upper panel) reveals that these bands differ mainly by their width. In contrast, comparing

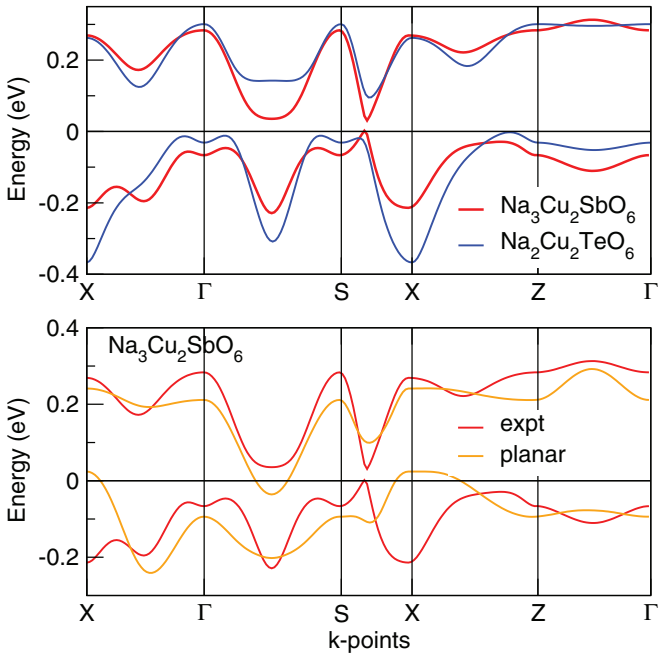

FIG. 7. (Color online) Top: LDA band structures showing the magnetically active antibonding $dp\sigma^*$ states for $Na_3Cu_2SbO_6$ and $Na_2Cu_2TeO_6$. Bottom: comparison of the LDA band structures calculated for different structural models of $Na_3Cu_2SbO_6$.

the antibonding $dp\sigma^*$ bands of $Na_3Cu_2SbO_6$ within the experimental crystal structure (distorted plaquettes) with the fictitious crystal structure (planar plaquettes) reveals similar bandwidths, but substantially different dispersions (compare X-Γ or X-Z in Fig. 7). The same trend is also observed for $Na_2Cu_2TeO_6$.

(i) To separate out the effect of the Sb↔Te substitution, we perform VCA calculations for the same structural model. In particular, a certain fraction x of Sb atoms is replaced by Te, with a concomitant change in the Na content, in order to keep the charge balance. The band structures calculated for different Te concentrations exhibit similar dispersions and similar bandwidth, evidencing the minor relevance of the pure substitutional effect for the magnetic exchange couplings [21].

To estimate the impact of the chain distortion and interatomic distances onto the magnetism in more detail, we evaluated the magnetic model also for two fictitious crystal structures of $Na_3Cu_2SbO_6$ and $Na_2Cu_2TeO_6$ (featuring planar dimer chains) [21]. The obtained hopping terms and exchange integrals are given in Tables III and V. LSDA + U calculations ($U_{3d} = 6 \pm 1$ eV) yield J_{1a}=−230 ± 50 K and $J_{1b} = 126 \pm 35$ K for the fictitious $Na_3Cu_2SbO_6$ and $J_{1a} = -312 \pm 80$ K and $J_{1b} = 212 \pm 45$ K for the fictitious $Na_2Cu_2TeO_6$, respectively. The dependence of the exchange integrals on the Coulomb repulsion U_{3d} is depicted in Fig. 6. Analysis of the resulting exchange couplings suggests that the two structural parameters act differently: the distortion of the dimer chains mainly influences the coupling strength of J_{1a} and the coupling regime between the dimer chains (t_{ic} and t_{il}), whereas the interdimer exchange J_{1b} is rather insensitive to this parameter (Table V), since the respective superexchange path does not involve O(2) atoms that rule the distortion.

(ii) Comparing the total exchange integrals for $Na_3Cu_2SbO_6$ for the experimental crystal structure with the planar system discloses an increase of the nearest-neighbor (NN) coupling J_{1a} by nearly a factor of 2, whereas J_{1b} is decreased by less than 20%. This observation is in line with the intuitive picture derived from geometrical considerations comparing the experimental distorted crystal structure to the

TABLE V. DFT estimates for the magnetic exchange integrals in $Na_3Cu_2SbO_6$ and $Na_2Cu_2TeO_6$. The AFM part of the exchange integral J_{1b}^{AFM} (in K) evaluated using the effective one-orbital model (with $U_{\mathrm{eff}} = 4$ eV) and total exchange integrals J_{1b} and J_{1a} (in K) from LSDA + U total energy calculations (using $U_{3d} = 6.0$ eV), for the experimental (expt.), the LDA-relaxed (relaxed), and the fictitious (planar) crystal structures.

Structure	J_{1a}	J_{1b}	(J_{1b}^{AFM})
	$Na_3Cu_2SbO_6$		
Expt.	−135	150	(188)
Relaxed	−125	162	(209)
Planar (expt.)	−230	126	(165)
Planar (relax.)	−227	142	(182)
	$Na_2Cu_2TeO_6$		
Expt.	−120	232	(305)
Relaxed	−122	197	(269)
Planar (expt.)	−312	212	(269)
Planar (relax.)	−305	200	(255)

fictitious system containing ideal planar chains (compare Fig. 1, lower panel). Locking the O atoms within the chain plane directly alters the exchange path of J_{1a} along Cu-O-Cu, by a change of the Cu-O-Cu bridging angle and the orientation of the magnetically active orbitals. In contrast, the superexchange path of J_{1b} (Cu-O-O-Cu) is altered only indirectly by changes of the crystal field due to the distortion of the Sb/TeO_6 octahedra (compare Fig. 1, lower panel).

(iii) The modulation of interatomic distances influences J_{1a} and J_{1b} in a similar way. The crucial impact of the interatomic distances on J_{1b} manifests itself in the coupling strength of the planar model structures for $Na_3Cu_2SbO_6$ and $Na_2Cu_2TeO_6$ (see Table V) with the corresponding next-nearest-neighbor (NNN) Cu-Cu interdimer distance. The about 0.1 Å shorter NNN Cu-Cu distance in the fictitious planar $Na_2Cu_2TeO_6$ structure compared to the fictitious planar $Na_3Cu_2SbO_6$ increases the coupling strength by about 60%. However, comparing the experimental distorted crystal structure with the planar model structure of $Na_2Cu_2TeO_6$ the difference in the NNN Cu-Cu distance is only half as large (about 0.05 Å) as between the two planar structures and result in about a 1/4 smaller increase of J_{1b}. Thus, J_{1b} follows a simple distance relation and scales according to r^2. The same relation holds for J_{1a} (compare J_{1a} for the two planar structures with the change of the NN Cu-Cu distance).

Based on the above considerations, we can conclude that the crucial parameter, determining the alteration ratio $\alpha = J_{1a}/J_{1b}$ for $Na_3Cu_2SbO_6$ and $Na_2Cu_2TeO_6$, is the distortion of the chains. Thus, a directed modification of the chain buckling by the appropriate substitution of ions should allow us to tune the magnetism of these systems. Furthermore, the chain distortion also influences the interchain coupling regime. In the experimental structure the long-range exchanges mostly operate within the magnetic layers (in the ab plane), whereas in the planar system the coupling between the layers is enhanced (t_{ij}'s in Table III).

V. ENERGY SPECTRUM

As already mentioned, the FM-AFM and AFM-AFM solutions correspond to different magnetic GSs. In the former case, the GS is similar to the Haldane chain and features sizable string order parameter $O_s = 0.36$, indicative of a topological order, while in the latter case the string order is suppressed ($O_s = 0.16$) [42]. It is thus tempting to find an observable quantity that would be substantially different in the two phases. Theoretical studies of the $S = 1/2$ AHC model suggest that this requirement is fulfilled for the momentum position of the spin gap. Indeed, the $Q = 0$ gap is characteristic for AFM-AFM chains, except for the narrow parameter range $\alpha = 0.79$–1.00, where the gap shifts to small finite $Q \leqslant 0.02/\pi$ [27]. In contrast, the spin gap in the FM-AFM chains is located at $Q = \pi$ [43]. Therefore, by measuring momentum resolved excitation spectra, the sign of J_{1a} can be reliably determined.

To resolve the ambiguity between the FM-AFM and AFM-AFM cases ultimately, we calculate the low-energy excitations for $\alpha = -1.25$ as well as $\alpha = 0.4$ using Lanczos diagonalization of the respective Heisenberg Hamiltonian. The resulting $E(Q)$ dependence is plotted in Fig. 8. Although

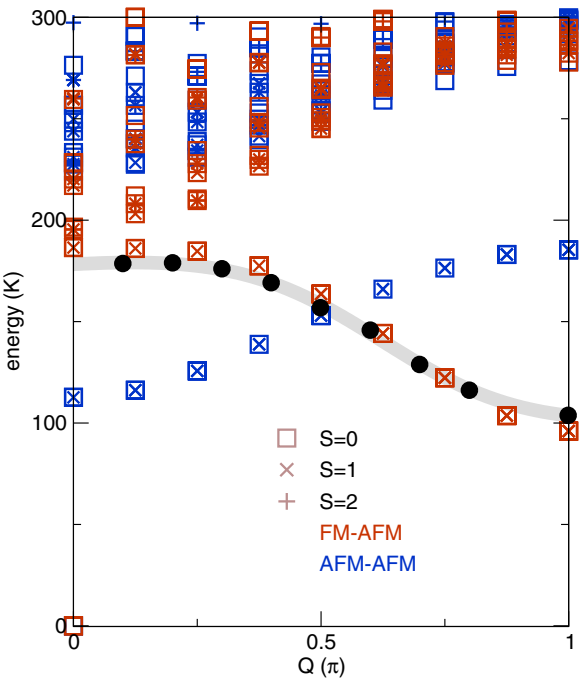

FIG. 8. (Color online) Low-energy excitation spectra for the alternating Heisenberg chains of $N = 32$ spins, corresponding to the QMC solutions (FM-AFM and AFM-AFM) from Table II. Note the difference in the behavior of the low-lying branch for the two solutions. Experimental data from Ref. [18] are shown with filled circles (the gray line is guide to the eye).

the two solutions yield similar estimates for the spin gap, its Q position is very different: $Q = \pi$ and $Q = 0$, for the FM-AFM and AFM-AFM solution, respectively. Another distinct feature of the excitation spectra is the well-separated branch of lowest-energy excitations (Fig. 8). For the FM-AFM solution, this branch resembles the behavior of $\cos(Q)$, while the AFM-AFM solution yields a $\sin(Q)$-like behavior.

To compare with the experimental dispersion from Ref. [18], we scale the two spectra using the values of the exchange couplings from our QMC fits to the magnetic susceptibility (Table II, last row). This way, we find that the FM-AFM solution agrees very well with the experimental data (Fig. 8), while the AFM-AFM solution can be safely ruled out.

Figure 8 also provides an answer to an intriguing question, why both $\alpha = -1.25$ and $\alpha = 0.4$ provide good fits to the susceptibility data. At finite temperature, magnetic susceptibility reflects the thermal-averaged magnetic spectrum integrated over the whole momentum space. Thus, at low temperatures, $\chi(T)$ is largely affected by the value of the spin gap, but is insensitive to its Q position. Since the values of the spin gap for the two solutions are very similar (around 100 K), the similarity of the low-temperature $\chi(T)$ is also not surprising. Moreover, the shape of the low-energy branch is similar (but reflected around $Q = \pi/2$), thus the Q-integrated spectrum is nearly the same in both cases. Only at elevated temperatures, the contribution of high-lying states gives rise to the difference in $\chi(T)$. This is in excellent agreement with the enhanced deviation of the AFM-AFM solution at high temperatures (Fig. 2, inset).

VI. SUMMARY

Since the first report on the magnetism of the low-dimensional $S = 1/2$ systems $Na_3Cu_2SbO_6$ and $Na_2Cu_2TeO_6$, their spin models were controversially debated in the literature. The main conundrum was the sign of the exchange coupling J_{1a} operating within the structural Cu_2O_6 dimers. To resolve the conflicting reports, we applied a series of different computational methods, including density functional theory (DFT) band structure, virtual crystal approximation, DFT + U, and hybrid functional calculations, as well as high-temperature series expansions, quantum Monte Carlo simulations, and exact diagonalization.

Our calculations evidence that the magnetism of both compounds can be described by the alternating Heisenberg chain model with two relevant couplings: ferromagnetic J_{1a} within the structural dimers, and antiferromagnetic J_{1b} between the dimers. The alternation parameter $\alpha = J_{1a}/J_{1b}$ amounts to about -1.25 and -0.55 in $Na_3Cu_2SbO_6$ and $Na_2Cu_2TeO_6$, respectively. This parameter regime corresponds to the Haldane phase, characterized by the gapped excitation spectrum and a topological string order.

Using extensive calculations for different structural models, we find that the physically relevant ratio $\alpha = J_{1a}/J_{1b}$ is primarily ruled by the distortion of the structural chains, while the Sb $\leftrightarrow$ Te substitution and the change in the Cu-Cu distance play a minor role. A comparison of the simulated dispersion $E(Q)$ with the experimental inelastic neutron-scattering data (Ref. [18]) yields an unequivocal evidence for the FM nature of J_{1a} in $Na_3Cu_2SbO_6$. These spectra facilitate the understanding of the similarity between the magnetic susceptibility curves for mutually exclusive solutions that involve ferromagnetic and antiferromagnetic J_{1a}.

It is important to note that the problem of ambiguous solutions appears in the empirical modeling, only. In contrast, the microscopic modeling based on DFT calculations readily yields a quasi-one-dimensional model with the ferromagnetic J_{1a}. This clearly indicates that present-day DFT calculations are a reliable tool to disclose even rather complicated cases and deliver a reliable microscopic magnetic model. Since the correctness of the magnetic model is of crucial importance for its refinement and extension, DFT calculations should be an indispensable ingredient of real-material studies.

ACKNOWLEDGMENTS

We are grateful to Professor M. Sato for explaining the details of his previous experimental work on $Na_3Cu_2SbO_6$ and $Na_2Cu_2TeO_6$. Fruitful discussions with A. A. Tsirlin are kindly acknowledged. O.J. was partially supported by the European Union through the European Social Fund (Mobilitas Grant No. MJD447). J.R. was supported by the DFG through the project RI 615/16-3.

[1] P. A. Lee, Rep. Prog. Phys. **71**, 012501 (2008).
[2] L. Balents, Nature (London) **464**, 199 (2010).
[3] J. S. Helton, K. Matan, M. P. Shores, E. A. Nytko, B. M. Bartlett, Y. Yoshida, Y. Takano, A. Suslov, Y. Qiu, J.-H. Chung, D. G. Nocera, and Y. S. Lee, Phys. Rev. Lett. **98**, 107204 (2007).
[4] S. Nakatsuji, K. Kuga, K. Kimura, R. Satake, N. Katayama, E. Nishibori, H. Sawa, R. Ishii, M. Hagiwara, F. Bridges, T. U. Ito, W. Higemoto, Y. Karaki, M. Halim, A. A. Nugroho, J. A. Rodriguez-Rivera, M. A. Green, and C. Broholm, Science **336**, 559 (2012).
[5] M. Isobe and Y. Ueda, J. Phys. Soc. Jpn. **65**, 3142 (1996); R. Valentí and T. Saha-Dasgupta, Phys. Rev. B **65**, 144445 (2002); A. Saúl and G. Radtke, Phys. Rev. Lett. **106**, 177203 (2011).
[6] J. Deisenhofer, R. M. Eremina, A. Pimenov, T. Gavrilova, H. Berger, M. Johnsson, P. Lemmens, H.-A. Krug von Nidda, A. Loidl, K.-S. Lee, and M.-H. Whangbo, Phys. Rev. B **74**, 174421 (2006); H. Das, T. Saha-Dasgupta, C. Gros, and R. Valentí, *ibid.* **77**, 224437 (2008); A. V. Ushakov and S. V. Streltsov, J. Phys.: Condens. Matter **21**, 305501 (2009).
[7] Y. Sasago, M. Hase, K. Uchinokura, M. Tokunaga, and N. Miura, Phys. Rev. B **52**, 3533 (1995); R. Valentí, T. Saha-Dasgupta, and C. Gros, *ibid.* **66**, 054426 (2002).
[8] M. Schmitt, A. A. Gippius, K. S. Okhotnikov, W. Schnelle, K. Koch, O. Janson, W. Liu, Y.-H. Huang, Y. Skourski, F. Weickert, M. Baenitz, and H. Rosner, Phys. Rev. B **81**, 104416 (2010).
[9] V. V. Mazurenko, M. V. Valentyuk, R. Stern, and A. A. Tsirlin, Phys. Rev. Lett. **112**, 107202 (2014).
[10] M. Jaime, V. F. Correa, N. Harrison, C. D. Batista, N. Kawashima, Y. Kazuma, G. A. Jorge, R. Stern, I. Heinmaa, S. A. Zvyagin, Y. Sasago, and K. Uchinokura, Phys. Rev. Lett. **93**, 087203 (2004); S. E. Sebastian, N. Harrison, C. D. Batista, L. Balicas, M. Jaime, P. A. Sharma, N. Kawashima, and I. R. Fisher, Nature (London) **441**, 617 (2006); S. Krämer, R. Stern, M. Horvatić, C. Berthier, T. Kimura, and I. R. Fisher, Phys. Rev. B **76**, 100406(R) (2007).
[11] M. Takigawa, T. Waki, M. Horvatić, and C. Berthier, J. Phys. Soc. Jpn. **79**, 011005 (2010).
[12] J. B. Goodenough, Phys. Rev. **100**, 564 (1955); J. Kanamori, J. Phys. Chem. Solids **10**, 87 (1959).
[13] W. E. Pickett, Rev. Mod. Phys. **61**, 433 (1989).
[14] Y. Miura, R. Hirai, Y. Kobayashi, and M. Sato, J. Phys. Soc. Jpn. **75**, 084707 (2006).
[15] S. Derakhshan, H. L. Cuthbert, J. E. Greedan, B. Rahaman, and T. Saha-Dasgupta, Phys. Rev. B **76**, 104403 (2007).
[16] M. Yamanaka, Y. Hatsugai, and M. Kohmoto, Phys. Rev. B **48**, 9555 (1993).
[17] H.-J. Koo and M.-H. Whangbo, Inorg. Chem. **47**, 128 (2008).
[18] Y. Miura, Y. Yasui, T. Moyoshi, M. Sato, and K. Kakurai, J. Phys. Soc. Jpn. **77**, 104709 (2008).
[19] J. Xu, A. Assoud, N. Soheilnia, S. Derakhshan, H. L. Cuthbert, J. E. Greedan, M. H. Whangbo, and H. Kleinke, Inorg. Chem. **44**, 5042 (2005).
[20] O. A. Smirnova, V. B. Nalbandyan, A. A. Petrenko, and M. Avdeev, J. Solid State Chem. **178**, 1165 (2005).
[21] See Supplemental Material at http://link.aps.org/supplemental/10.1103/PhysRevB.89.174403 for the crystal structures, full set of transfer integrals, dependence of the exchange integrals on the structural model, temperature dependence of magnetic susceptibility as a function of oxygen deficiency, as well as auxiliary DOS and band-structure plots.

[22] K. Koepernik and H. Eschrig, Phys. Rev. B **59**, 1743 (1999).
[23] J. P. Perdew and Y. Wang, Phys. Rev. B **45**, 13244 (1992).
[24] D. Kasinathan, M. Wagner, K. Koepernik, R. Cardoso-Gil, Y. Grin, and H. Rosner, Phys. Rev. B **85**, 035207 (2012).
[25] J. Heyd, G. E. Scuseria, and M. Ernzerhof, J. Chem. Phys. **118**, 8207 (2003); **124**, 219906 (2006).
[26] G. Kresse and J. Furthmüller, Phys. Rev. B **54**, 11169 (1996); Comput. Mater. Sci. **6**, 15 (1996).
[27] D. C. Johnston, R. K. Kremer, M. Troyer, X. Wang, A. Klümper, S. L. Bud'ko, A. F. Panchula, and P. C. Canfield, Phys. Rev. B **61**, 9558 (2000).
[28] J. J. Borras-Almenar, E. Coronado, J. Curely, R. Georges, and J. C. Gianduzzo, Inorg. Chem. **33**, 5171 (1994).
[29] S. Todo and K. Kato, Phys. Rev. Lett. **87**, 047203 (2001).
[30] A. Albuquerque, F. Alet, P. Corboz, P. Dayal, A. Feiguin, S. Fuchs, L. Gamper, E. Gull, S. Gürtler, A. Honecker, R. Igarashi, M. Körner, A. Kozhevnikov, A. Läuchli, S. R. Manmana, M. Matsumoto, I. P. McCulloch, F. Michel, R. M. Noack, G. Pawlowski, L. Pollet, T. Pruschke, U. Schollwöck, S. Todo, S. Trebst, M. Troyer, P. Werner, and S. Wessel, J. Magn. Magn. Mater. **310**, 1187 (2007).
[31] J. Schulenburg, http://www-e.uni-magdeburg.de/jschulen/spin.
[32] A. A. Belik, M. Azuma, and M. Takano, J. Solid State Chem. **177**, 883 (2004).
[33] O. Volkova, I. Morozov, V. Shutov, E. Lapsheva, P. Sindzingre, O. Cépas, M. Yehia, V. Kataev, R. Klingeler, B. Büchner, and A. Vasiliev, Phys. Rev. B **82**, 054413 (2010).
[34] J. W. Hall, W. E. Marsh, R. R. Weller, and W. E. Hatfield, Inorg. Chem. **20**, 1033 (1981).
[35] M. Schmitt, J. Málek, S.-L. Drechsler, and H. Rosner, Phys. Rev. B **80**, 205111 (2009).
[36] A. U. B. Wolter, F. Lipps, M. Schäpers, S.-L. Drechsler, S. Nishimoto, R. Vogel, V. Kataev, B. Büchner, H. Rosner, M. Schmitt, M. Uhlarz, Y. Skourski, J. Wosnitza, S. Süllow, and K. C. Rule, Phys. Rev. B **85**, 014407 (2012).
[37] F. Fuchs, J. Furthmüller, F. Bechstedt, M. Shishkin, and G. Kresse, Phys. Rev. B **76**, 115109 (2007).
[38] O. K. Andersen and T. Saha-Dasgupta, Phys. Rev. B **62**, R16219 (2000).
[39] O. K. Andersen and O. Jepsen, Phys. Rev. Lett. **53**, 2571 (1984).
[40] Different DFT codes employ different basis sets, hence the resulting band structures are not identical. For an instructive example, see H. Rosner, M. Schmitt, D. Kasinathan, A. Ormeci, J. Richter, S.-L. Drechsler, and M. D. Johannes, Phys. Rev. B **79**, 127101 (2009).
[41] E. R. Ylvisaker, W. E. Pickett, and K. Koepernik, Phys. Rev. B **79**, 035103 (2009).
[42] S. Watanabe and H. Yokoyama, J. Phys. Soc. Jpn. **68**, 2073 (1999).
[43] K. Hida, J. Phys. Soc. Jpn. **63**, 2514 (1994).